Supplementary Information

Note S1. System Operation Flow

Wireless charging circuit The wireless charging circuit consists of a full-wave rectifier (FWR), low-dropout-regulator (LDO), a Schottky diode, and power-management circuit for charging (PMIC-C) the battery. The FWR converts the input 13.56 MHz alternating current (AC) from the coil to direct current (DC). The LDO regulates the DC input to 5 V (~10 mA) DC output. The DC output flows through the Schottky diode and delivers the charges to PMIC-C. The PMIC-C, then, regulates the power to charges the Li-ion battery according to the voltage level of the battery.

System power management The power from Li-ion battery goes through the DC/DC converter that regulates it to 3.2 V (~2 mA) and delivers to the active components throughout the system, which includes a microcontroller (MCU), accelerometer, and flash memory.

Device operation The user interface controls the device operation. To turn on the system, it first connects to the device. By default, the accelerometer digitally senses 3-axis 1600 Hz accelerometer data and the device streams the 20 Hz downsampled data to the phone along with its battery level without saving the data to the on-board memory. Using the blue "Start Session" and the red "Stop Session" button, the user interface starts and stops recording the data to an on-board flash memory within the device and the recording status toggles accordingly (Fig. 1c). When the session begins, the MCU receives the data from the accelerometer and writes it to the 2 Gb flash memory. During the recording session, pressing the event logging buttons mark the time of specific incidents, arbitrarily assigned to each button. When the session ends, the user interface downloads the data from the device via Bluetooth. The interface can also control multiple devices simultaneously and in time synchronized manner.

Note S2. Finite element analysis

The commercial software ABAQUS (ABAQUS Analysis User's Manual 2010, V6.10) was used to design the device and optimize its mechanical performance. The objectives are to ensure that (1) the Cu layer in the interconnects remains elastic, i.e., no plastic deformation, and (2) minimize the normal and shear stresses on the human skin to achieve a low somatosensory perception when the device undergoes different types of external loads (stretching, bending, and twisting). The epoxy, silicone elastomer (Ecoflex), and silicone gel were modeled by hexahedron elements (C3D8R) while the thin Cu layer and PI films were modeled by composite shell elements (S4R). The number of elements in the model was ~2×10^7, and the minimal element size was 1/8 of the width of the narrowest interconnects (100 μm). The mesh convergence of the simulation was guaranteed for all cases. The elastic modulus (E) and Poisson's ratio (v) are E_{Cu}=119 GPa, v_{Cu} =0.34, E_{PI} =2.5 GPa, v_{PI} =0.34, E_{Gel} =5 kPa, v_{Gel} =0.49, E_{Ecoflex} =60 kPa, $v_{Ecoflex}$ =0.49, E_{Epoxy} =22 GPa and v_{Epoxy} =0.32.

Note S3. The theoretical vibration model of a one-dimensional rod with damping

For one-dimensional vibration of a viscoelastic rod, the displacement takes the form $u=f(x)e^{i\omega t}$, where t is time, ω is the angular frequency, and $f(x)$ depends on the x coordinate. The relation between strain ε and displacement u, constitutive model (Kelvin-Voigt model), and dynamic equation of motion are

$$\varepsilon = \frac{\partial u}{\partial x} \tag{1}$$

$$\begin{aligned}\sigma &= E\varepsilon + \eta\frac{\partial \varepsilon}{\partial t} \\ &== \left(E + \mathrm{i}\omega\eta\right)\frac{\partial u}{\partial x}\end{aligned} \tag{2}$$

$$\frac{\partial \sigma}{\partial x} = \rho\frac{\partial^2 u}{\partial t^2} \tag{3}$$

respectively, where σ is the stress, and E, ρ and η are the Young's modulus, mass density, and viscoelastic damping coefficient, respectively.

Substitution of Eq. (2) into Eq. (3) gives

$$\frac{\partial^2 u}{\partial x^2} = \frac{1}{c^2}\frac{\partial^2 u}{\partial t^2} \tag{4}$$

where

$$c=\sqrt{\frac{E+i\omega\eta}{\rho}} \tag{5}$$

For the problem shown in Fig. S7, the displacement and stress boundary conditions at $x=0$ and $x=L$ are given by

$$\begin{cases} u\left(0,t\right)=u_0e^{\mathrm{i}\Omega t} \\ \sigma\left(L,t\right)=-M\left.\dfrac{\partial^2u\left(x,t\right)}{\partial t^2}\right|_{x=L} \end{cases} \tag{6}$$

where u_0 and Ω are the magnitude and the angular frequency of the excitation load (from the vibration platform) applied to the rod at $x=0$. M is the mass per unit area, which represents the mass of the device over the area of its bottom layer

The Fourier transform

$$\begin{aligned} \hat{u}\left(x,\omega\right)&=\int_{-\infty}^{+\infty}u\left(x,t\right)e^{-\mathrm{i}\omega t}\mathrm{d}t \\ u\left(x,t\right)&=\frac{1}{2\pi}\int_{-\infty}^{+\infty}\hat{u}\left(x,\omega\right)e^{\mathrm{i}\omega t}\mathrm{d}\omega \end{aligned} \tag{7}$$

applied to Eq. (4) gives

$$\frac{\mathrm{d}^2\hat{u}}{\mathrm{d}x^2}+k^2\hat{u}=0 \tag{8}$$

where $k=\dfrac{\omega}{c}$. The boundary conditions in Eq. (6) become

$$\begin{cases} \hat{u}\left(0,\omega\right)=2\pi u_0\delta\left(\omega-\Omega\right) \\ \hat{\sigma}\left(L,\omega\right)=-M\left(-\mathrm{i}\omega\right)^2\hat{u}\left(L,\omega\right)=M\omega^2\hat{u}\left(L,\omega\right) \end{cases} \tag{9}$$

where $\delta\left(x\right)$ is the Dirac Delta function.

The solution of Eq. (8) is

$$\begin{aligned} \hat{u}\left(x,\omega\right)&=C_1e^{\mathrm{i}kx}+C_2e^{-\mathrm{i}kx} \\ \hat{\sigma}\left(x,\omega\right)&=\mathrm{i}k\left(E+\mathrm{i}\omega\eta\right)\left(C_1e^{\mathrm{i}kx}-C_2e^{-\mathrm{i}kx}\right) \end{aligned} \tag{10}$$

where the coefficients C_1 and C_2 are determined by the boundary conditions (9) to (10) as

$$\begin{cases} C_1=\dfrac{\left[\mathrm{i}k\left(E+\mathrm{i}\omega\eta\right)+M\omega^2\right]e^{-\mathrm{i}kL}\pi u_0\delta\left(\omega-\Omega\right)}{\mathrm{i}k\left(E+\mathrm{i}\omega\eta\right)\cos\left(Lk\right)-\mathrm{i}M\omega^2\sin\left(Lk\right)} \\ C_2=\dfrac{\left[\mathrm{i}k\left(E+\mathrm{i}\omega\eta\right)-M\omega^2\right]e^{\mathrm{i}kL}\pi u_0\delta\left(\omega-\Omega\right)}{\mathrm{i}k\left(E+\mathrm{i}\omega\eta\right)\cos\left(Lk\right)-\mathrm{i}M\omega^2\sin\left(Lk\right)} \end{cases} \tag{11}$$

Substituting Eq. (11) into Eq. (10) yields

$$\hat{u}\left(x,\omega\right)=\left\{\begin{aligned} &\frac{\left[\mathrm{i}k\left(E+\mathrm{i}\omega\eta\right)+M\omega^2\right]e^{-\mathrm{i}kL}e^{\mathrm{i}kx}}{\mathrm{i}k\left(E+\mathrm{i}\omega\eta\right)\cos\left(Lk\right)-\mathrm{i}M\omega^2\sin\left(Lk\right)} \\ &+\frac{\left[\mathrm{i}k\left(E+\mathrm{i}\omega\eta\right)-M\omega^2\right]e^{\mathrm{i}kL}e^{-\mathrm{i}kx}}{\mathrm{i}k\left(E+\mathrm{i}\omega\eta\right)\cos\left(Lk\right)-\mathrm{i}M\omega^2\sin\left(Lk\right)} \end{aligned}\right\}\pi u_0\delta\left(\omega-\Omega\right) \tag{12}$$

The Fourier Transform of the acceleration $a\left(x,t\right)=\partial^2u\left(x,t\right)/\partial t^2$ is

$$\hat{a}\left(x,\omega\right)=\left(-\mathrm{i}\omega\right)^2\hat{u}\left(x,\omega\right) \tag{13}$$

Its inverse transform gives the acceleration

$$a(x,t)=\frac{1}{2\pi}\int_{-\infty}^{+\infty}\left\{-\pi u_0\omega^2\delta(\omega-\Omega)\left[\begin{array}{l}\dfrac{\left[\mathrm{i}k(E+\mathrm{i}\omega\eta)+M\omega^2\right]e^{-\mathrm{i}kL}e^{\mathrm{i}kx}}{\mathrm{i}k(E+\mathrm{i}\omega\eta)\cos(Lk)-\mathrm{i}M\omega^2\sin(Lk)}\\+\dfrac{\left[\mathrm{i}k(E+\mathrm{i}\omega\eta)+M\omega^2\right]e^{\mathrm{i}kL}e^{-\mathrm{i}kx}}{\mathrm{i}k(E+\mathrm{i}\omega\eta)\cos(Lk)-\mathrm{i}M\omega^2\sin(Lk)}\end{array}\right]\right\}e^{\mathrm{i}\omega t}\mathrm{d}\omega \tag{14}$$

which can be further expressed as

$$a(x,t)=-u_0\Omega^2e^{\mathrm{i}\Omega t}\left\{\frac{\sqrt{(E+\mathrm{i}\omega\eta)\rho}\cos\left[\dfrac{(x-L)}{c}\Omega\right]+M\Omega\sin\left[\dfrac{(x-L)}{c}\Omega\right]}{\sqrt{(E+\mathrm{i}\omega\eta)\rho}\cos\left(\dfrac{L}{c}\Omega\right)-M\Omega\sin\left(\dfrac{L}{c}\Omega\right)}\right\} \tag{15}$$

The acceleration at the x=L is

$$a(L,t)=\frac{-u_0\Omega^2e^{\mathrm{i}\Omega t}\left(\dfrac{L}{c}\Omega\right)}{\left(\dfrac{L}{c}\Omega\right)\cos\left(\dfrac{L}{c}\Omega\right)-\left(\dfrac{LM\Omega^2}{E+\mathrm{i}\omega\eta}\right)\sin\left(\dfrac{L}{c}\Omega\right)} \tag{16}$$

For the displacement at the other end $x=0$ to take the form $u(0,t)=\mathrm{Re}\left\{u_0e^{\mathrm{i}\Omega t}\right\}=u_0\cos(\Omega t)$, the above acceleration at the end x=L is simplified to

$$a(L,t)=\mathrm{Re}\left\{\frac{-u_0\Omega^2e^{\mathrm{i}\Omega t}\left(\dfrac{L}{c}\Omega\right)}{\left(\dfrac{L}{c}\Omega\right)\cos\left(\dfrac{L}{c}\Omega\right)-\left(\dfrac{LM\Omega^2}{E+\mathrm{i}\omega\eta}\right)\sin\left(\dfrac{L}{c}\Omega\right)}\right\} \tag{17}$$

Note S4. Motion artifact suppression in respiration analysis based on wavelet coherence

In the approach reported in the main text, the continuous wavelet transform (CWT) subtraction algorithm aims to exploit time-synchronized three-axis acceleration measurements to extract respiration signal at all activity levels. The detection mechanism relies critically on the suprasternal notch (SN) mounting location and orientation, where the z-axis and x-axis measurements are both sensitive to chest-wall motion, while the y-axis acceleration is mainly associated with core-body motions. The goal is to find the common mode between z-axis and x-axis motion but differential mode between z-axis and y-axis motion.

The wavelet cross spectrum of two time series, x_n and y_n, where $n=1,2,\ldots,N$ is:

$$C_{xy}(b,n)=C_x^*(b,n)C_y(b,n) \tag{18}$$

where $C_x(b,n)$ and $C_y(b,n)$ denotes the CWT of x and y at scales b and positions n. The superscript denotes the complex conjugate. The coherence projection for the common mode signal embedded in y_n becomes,

$$C_{y'}(b,n)=\frac{C_{xy}^*(b,n)}{C_{xx}(b,n)}\cdot C_x(b,n) \tag{19}$$

We kept wavelet transform coefficients with wavelet coherence $R_{xy}^2(b,n)>0.8$, where

$$R_{xy}^2(b,n)=\frac{\left|C_x^*(b,n)C_y(b,n)\right|^2}{|C_x(b,n)|^2\left|C_y(b,n)\right|^2} \tag{20}$$

For the specific application in suppressing motion artifacts occurring in the frequency range of respiration cycles, the computation uses Morlet wavelets. We chose a sampling period $\Delta t=20\ s$ to cover all time scale of interest. The smallest scale for the Morlet wavelets is $s_0=2\Delta t$. The CWT discretizes scales with 16 voices per octave. The number of octaves is set to be the nearest integer less than or equal to $\log_2 N-1$, which in this case is 10. We perform the continuous wavelet transforms as well as a smoothing operation over 16 scales using the built-in MATLAB™ function “cwt” and “smoothCFS”.

In practice, the wavelet transform projection yields common mode z' values between z- and x-axis measurements. The differential mode z'' between z' and y-axis measurements decouple motions from respiration, according to

$$C_{z'} = \frac{C_{xz}}{C_{zz}} \cdot C_{z,} \tag{21.1}$$

$$C_{z''} = \left(1 - \frac{C_{yz'}}{C_{z'z'}}\right) \cdot C_{z'}. \tag{21.2}$$

Fig. S22a demonstrates an application of the algorithm to simulated signals. Two time-series data, x and z are generated. Both data carry a large amplitude chirp signal in common to mimic the time non-stationary motion artifact, as well as a random gaussian noise of same distribution. A differential sinusoidal signal is added to z to simulate the respiration signal. The algorithm detects the common mode chirp signal between x and z and recovers the differential sinusoidal signal with gaussian noise in z. Fig. S22b presents the subtraction results from sample experimental measurement, using the three-axis acceleration data acquired from a healthy-normal subject during walking. The algorithm suppresses the fast motion artifacts and recovers the slower respiration patterns. Fig. S22c shows a sample detection for zero-crossing nodes using sample extracted respiration signal. A dynamic threshold, set as a tenth of the standard deviation of data collected for 1 min, eliminates the effects of small-amplitude ripples that appear on top of the general respiration pattern.

Note S5. Detection of Body Orientation

We analyze body orientation in SO(3) by finding the rotation matrix transforming the nominal gravity vector in the canonical frame $\boldsymbol{g} = [0,0,g_0]$ to the gravity vector measured in the device frame $\boldsymbol{g'} = [a_x, a_y, a_z]$, where the magnitude of gravity is estimated as $g_0 = \sqrt{a_x^2 + a_y^2 + a_z^2}$. We use Rodrigues' rotation formula for computation efficiency[61],

$$\boldsymbol{v}_{rot} = \boldsymbol{v}\cos\theta + (\boldsymbol{k} \times \boldsymbol{v})\sin\theta + \boldsymbol{k}(\boldsymbol{k} \cdot \boldsymbol{v})(1 - \cos\theta) \tag{22}$$

where $\boldsymbol{k}$ is the unit vector representing the rotation axis around which vector $\boldsymbol{v}$ rotate an angle θ following right-hand rule. Eq. 22 can be represented in matrix notation, $\boldsymbol{v}_{rot} = \boldsymbol{R}\boldsymbol{v}$, where $\boldsymbol{R}$ is the rotation matrix,

$$\boldsymbol{R} = \boldsymbol{I} + (\sin\theta)\boldsymbol{K} + (1 - \cos\theta)\boldsymbol{K}^2 \tag{23}$$

In the above equation, $\boldsymbol{I}$ is the 3 × 3 identity matrix, $\boldsymbol{K}$ is the skew-symmetric cross-product matrix of $\boldsymbol{k} = [k_1, k_2, k_3]$,

$$\boldsymbol{K} = \begin{bmatrix} 0 & -k_3 & k_2 \\ k_3 & 0 & -k_1 \\ -k_2 & k_1 & 0 \end{bmatrix} \tag{24}$$

Given the two gravity vectors $\boldsymbol{g}$ and $\boldsymbol{g'}$, we compute rotation axis and angle using cross product and dot product of normalized vectors $\hat{\boldsymbol{g}}$ and $\widehat{\boldsymbol{g'}}$,

$$\boldsymbol{k} = \frac{\hat{\boldsymbol{g}} \times \widehat{\boldsymbol{g'}}}{\left|\hat{\boldsymbol{g}} \times \widehat{\boldsymbol{g'}}\right|}, sin\theta = \left|\hat{\boldsymbol{g}} \times \widehat{\boldsymbol{g'}}\right|, \cos\theta = \hat{\boldsymbol{g}} \cdot \widehat{\boldsymbol{g'}}. \tag{25}$$

If we let $\boldsymbol{K'}$ be the skew symmetric matrix of $\hat{\boldsymbol{g}} \times \widehat{\boldsymbol{g'}}$, *i.e.* $\boldsymbol{K'} = \left|\hat{\boldsymbol{g}} \times \widehat{\boldsymbol{g'}}\right|\boldsymbol{K}$. Substituting all expressions to Eq. 23, we obtain rotation matrix,

$$\boldsymbol{R} = \boldsymbol{I} + \boldsymbol{K'} + \frac{\left(1 - \hat{\boldsymbol{g}} \cdot \widehat{\boldsymbol{g'}}\right)\boldsymbol{K'}^2}{\left|\hat{\boldsymbol{g}} \times \widehat{\boldsymbol{g'}}\right|^2} \tag{26}$$

We convert the rotation matrix to the corresponding Euler angles in the device frame using MATLAB™ function "rotm2eul". The rotation angle around the longitudinal axis of body indicates the body orientation of major interest in the sleep study.

Note S6. Hidden Markov Model with Gaussian Mixture Emissions

Sleep scoring involves modeling time series sequences with discrete states. Markov chains are one of the most straightforward statistical approaches to determine the likelihood of a sequence of states. Realistically, MA signal features would not tell sleep stages deterministically. We introduce Hidden Markov Model with Gaussian mixture emissions (GMMHMM) to capture the stochastic emission from states to observations. A Hidden Markov Model (HMM) $\boldsymbol{\Phi} = (\boldsymbol{A}, \boldsymbol{B}, \pi)$ encodes a joint probability distribution of generative states sequences $\boldsymbol{\Omega} = \{1, 2, 3, \dots, N\}$ characterized by a set of output observation symbols $\boldsymbol{O} = \{o_1, o_2, \dots, o_M\}$ with an underlying probabilistic dependence. We let s_t denote the state at time t. In the mathematical representation, $\boldsymbol{A} = \{p_{ij}\}$ is a transition probability matrix, where p_{ij} is the transition probability from state i to j. $\boldsymbol{B} = \{q_{ik}\}$ is the output probability distribution, where q_{ik} is the probability of

emitting observation symbol o_k in state i. $\pi = P(s_0 = i)$ is the initial state distribution. Sleep stage identification is a learning problem, *i.e.* given a sequence of observations $\boldsymbol{X} = (X_1, X_2, \ldots X_T)$, to find the best characteristic model parameter $\boldsymbol{\Phi}'$ so that the joint probability $\prod P(X|\Phi)$ is optimized through expectation-maximization (EM) algorithm. For the specific application, we use sklearn.hmm.GMMHMM module to train the HMM parameters and infer the hidden states. We randomly initialize the HMM parameter values. The prior distribution over initial states is uniform. The EM algorithm runs for 10 iterations or until convergence.

In the sleep study, the input features to the GMMHMM model take the form of multi-frequency band signal power, characterized by the band-limited root mean square (BLRMS) in 120-s time epoch, as our input features to the GMMHMM model. The band choices feature the 0.1-0.8 Hz respiration signals, as well as the 20-50 Hz cardiac signals. We choose in total seven bands for a balance between the characterization of system complexity and the feature representation for generality. Fig. S16a shows the full feature extraction filter-bank. Fig. S16b shows the time-series of each band power for the sample 7-hour sleep data presented in the main text, Fig. 5.

For the HMM model, we set the number of states to be $N = 5$. Multi-band z-axis signal power on a logarithmic scale serves as the observable clustering features to classify the five sleep stages labeled as 0 to 4 from Wake to Rapid Eye Movement (REM). The multi-band choices are 0.1-0.8 Hz for respiration, sub-bands in the range 0.8-20 Hz for body motions, and 20-80 Hz for cardiac activity. Gaussian mixture emissions determine the probability of multi-band power observations given the state. The inferred hidden states capture the overall trend of clinician determined sleep scoring.

The HMM model developed upon small dataset is a simple clustering method providing no information about the labeling. We permute the inferred states for all combinations of labeling and assign each class to a stage according to a minimum marathon distance optimization. Fig. S16c presents the final classification result in comparison with the clinically determined sleep stages. Fig. S16c summarizes the success rate in a confusion matrix.

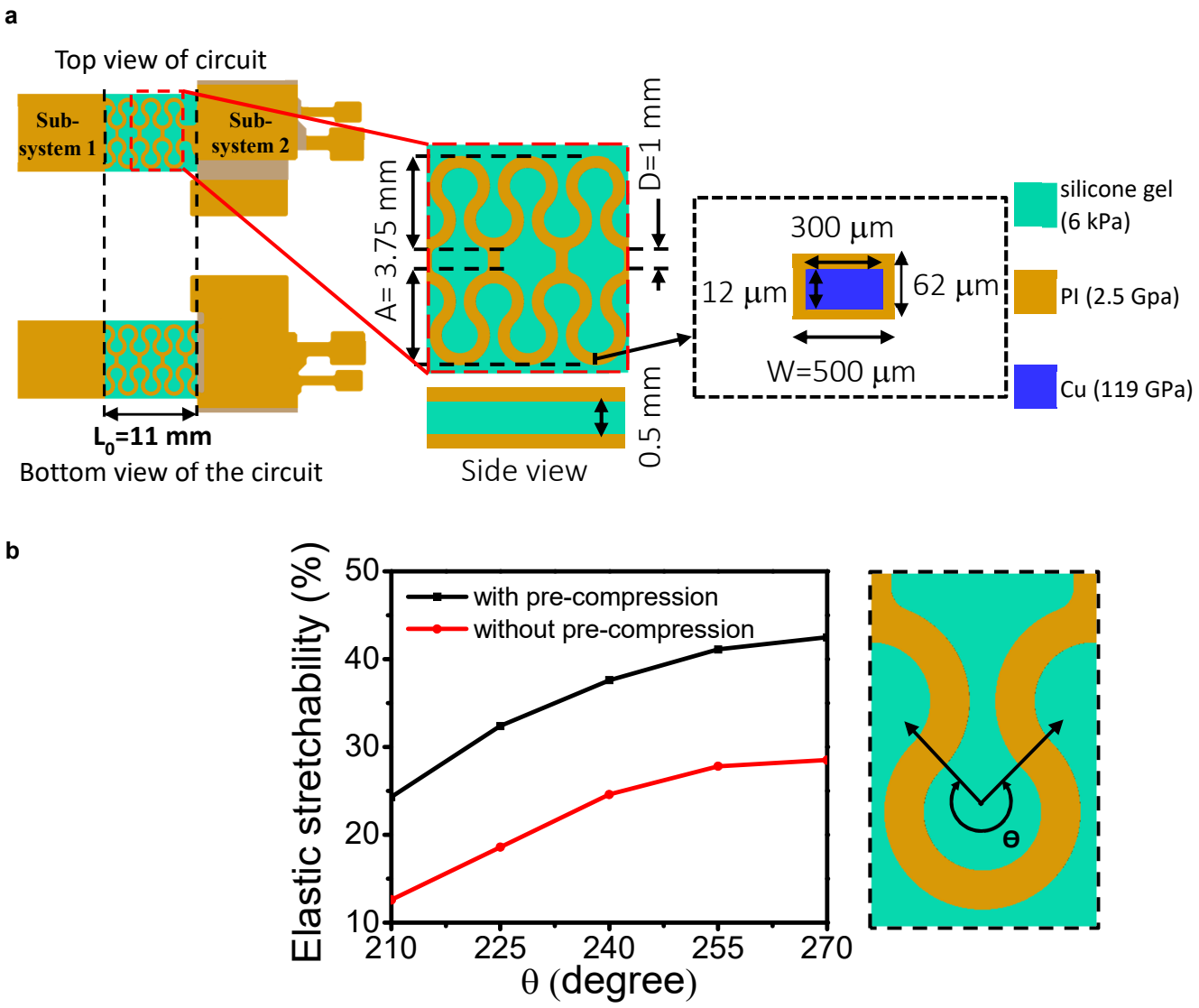

Fig. S1. Optimized mechanical designs for the electrical interconnects. (a) Schematic illustration of a double layer serpentine interconnect with an arc angle of 270º **(b)** Relationship between the arc angle and the elastic stretchability of the interconnects with and without pre-compression.

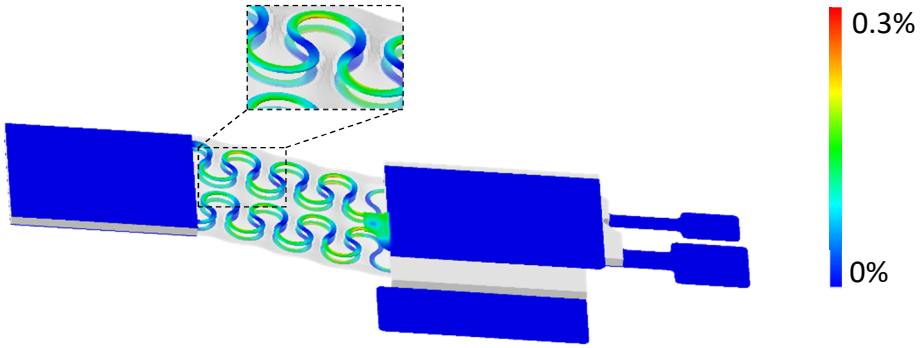

Fig. S2.The strain distribution in the Cu layer of the interconnect after stretching to 11 mm. The interconnects straighten back to their nominal (non-buckled) length from the pre-buckled state at 11% strain of the overall device.

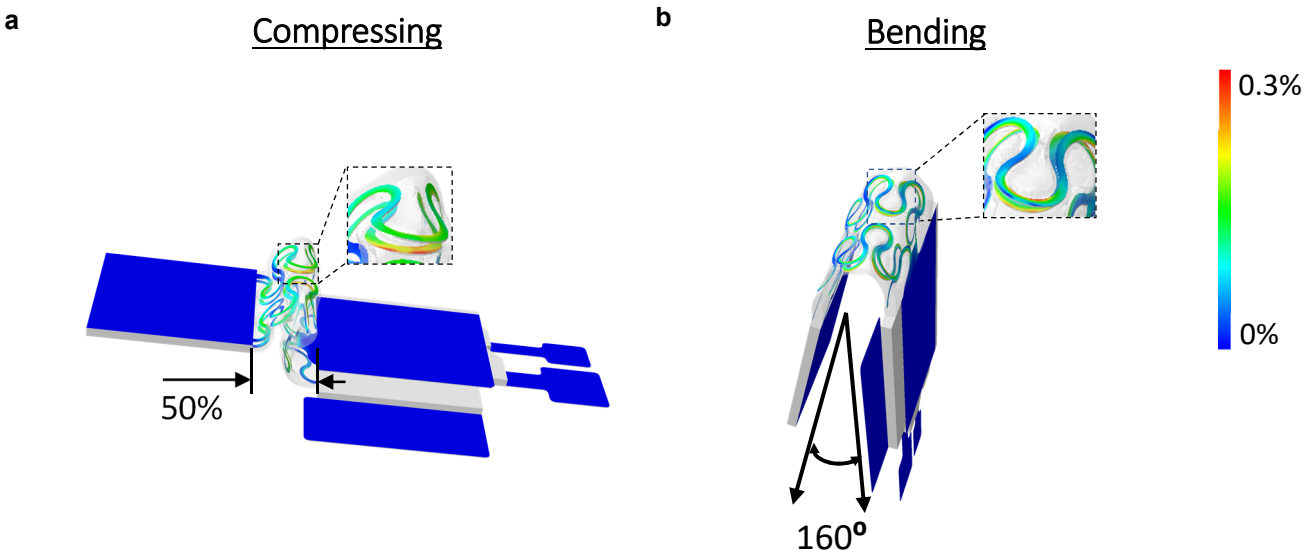

Fig. S3.The strain distribution in the Cu layer for the device after deformations. (a) 50% compression and **(b)** 160° bending angle. For both loading cases, the computed strain in the Cu layer of interconnects is lower than the 0.3% yielding strain

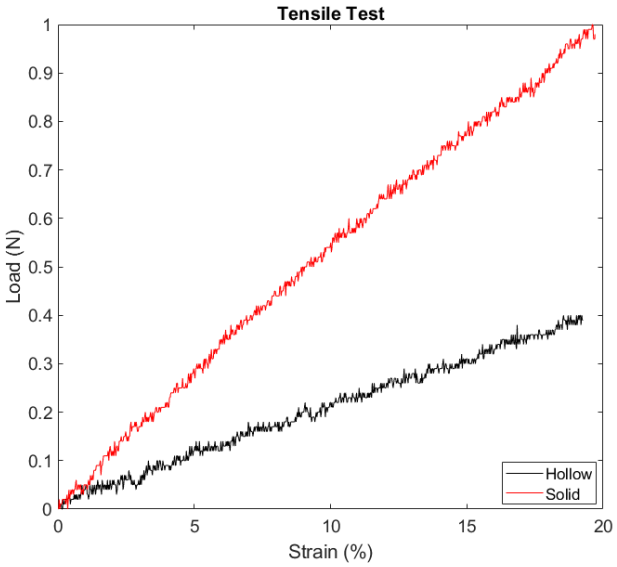

Fig. S4. Mechanical testing of the devices with hollow and solid silicone elastomer enclosure. The solid silicone elastomer enclosure is much stiffer than the hollow enclosure under tension.

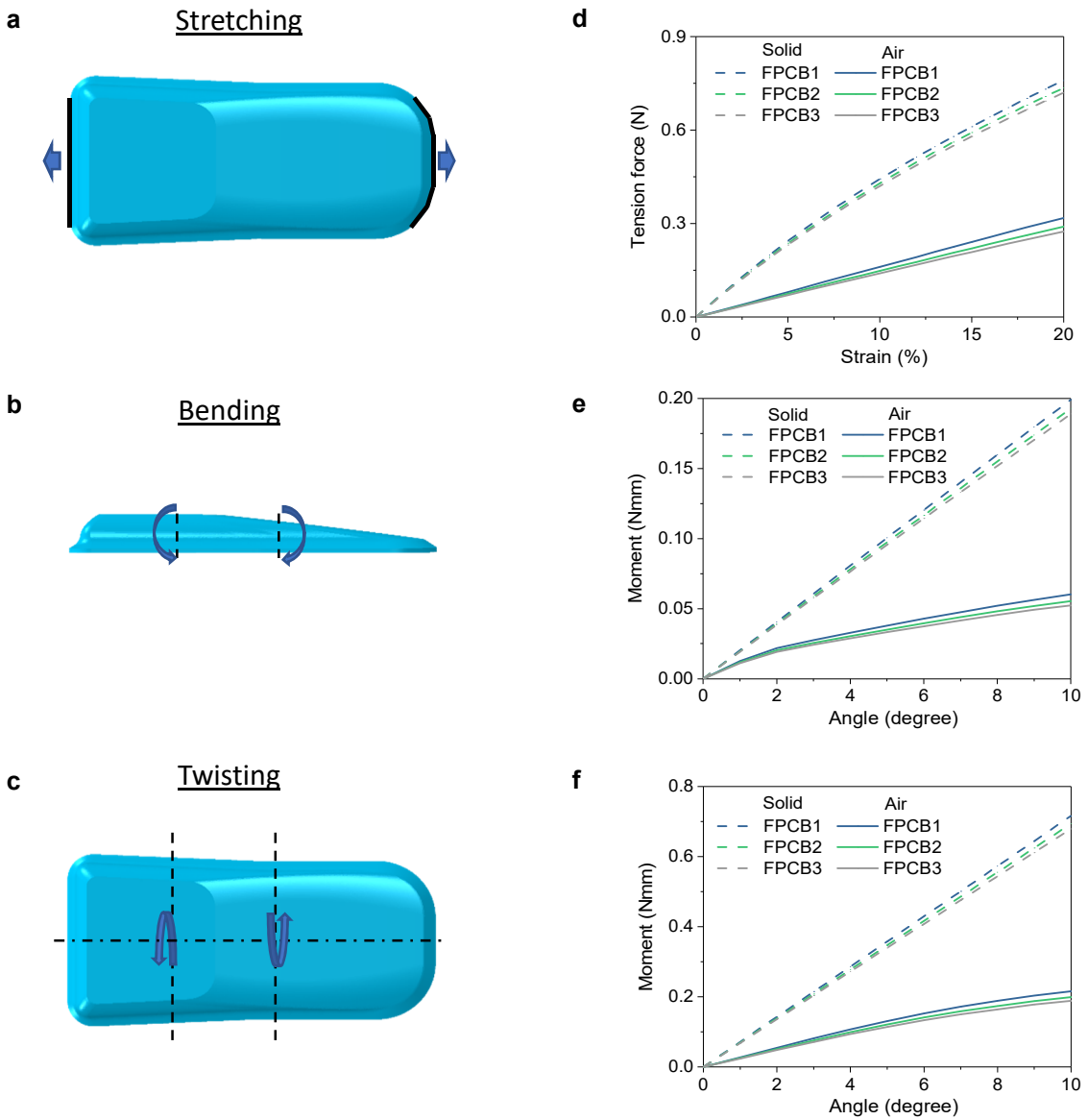

Fig. S5.FEA results of the devices with different FPCBs thicknesses under different modes of mechanical loading. Illustration of device under different modes of load: **(a)** stretching, **(b)** bending, and **(c)** twisting on the devices with different FPCBs thicknesses (FPCB1: 12 μm PI/ 25 μm Cu/ 12 μm PI; FPCB2: 8.69 μm PI/ 20 μm Cu/ 8.69 μm PI; FPCB2: 5.79 μm PI/ 12.5 μm Cu/ 5.79 μm PI). **(d)** Tensile force as a function of the applied strain for the solid and hollow package with a 61 kPa and 18 kPa equivalent tensile modulus for the devices with FPCB1 respectively. **(e)** Moment as a function of the bending angle for the solid and hollow package configurations with a 11 Nmm^2 and 6.8 Nmm^2 equivalent bending stiffness for the devices with FPCB1 respectively. **(f)** Moment as a function of the twisting angle for the solid and hollow package configurations with a 38 Nmm^2 and 15 Nmm^2 equivalent twisting stiffness for the devices with FPCB1 respectively. The results for stretching, bending, and twisting deformation show that the thickness of the layers has a small influence (less than 10% difference) in the equivalent tensile modulus, bending, and twisting stiffness for these three FPCBs.

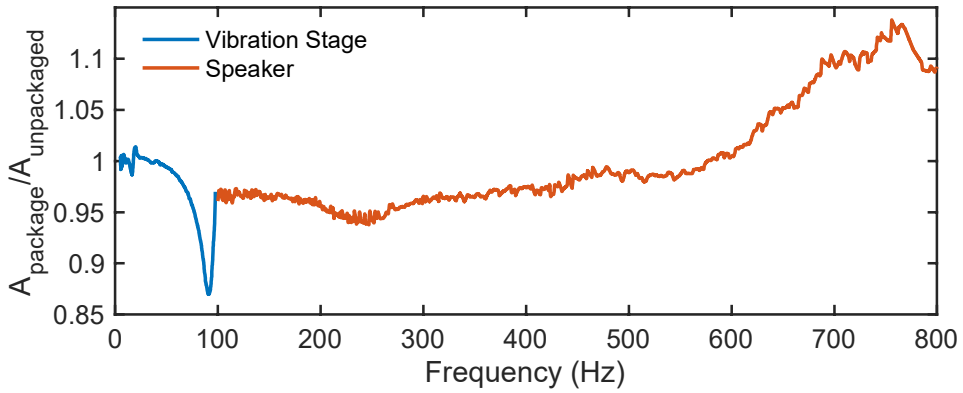

Fig. S6. Experimental comparison between the frequency responses of a hollow packaged device and a mechanically independent accelerometer. The ratio between the frequency response of a hollow packaged device $A_{packaged}$ and that of an unpackaged accelerometer $A_{unpackaged}$ stays close to 1 in the frequency range of interest (0-800 Hz), except for a maximum of ~13% drop in the relative response around 91 Hz due likely to a resonance; the encapsulated device is more sensitive than the unpackaged one at high frequencies (>600 Hz). The driving sources for the frequency sweep tests are a vibration stage (3B, Scientific) (1-100 Hz) and a speaker (100-800 Hz).

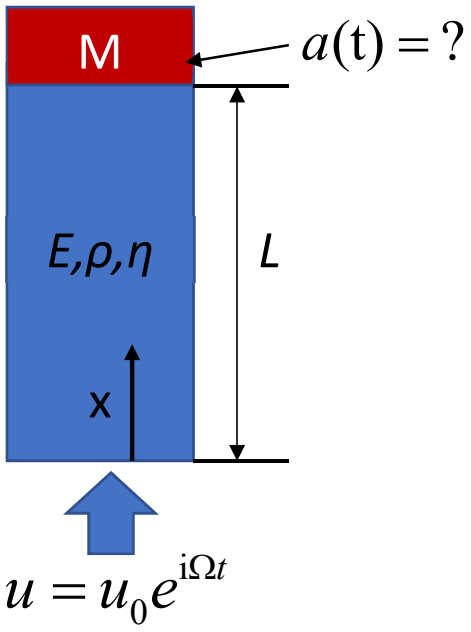

Fig. S7.Schematic illustration of the vibration model of a one-dimensional rod with damping. The parameters of the model are described next. E, ρ and η are the Young's modulus, mass density and damping coefficient, respectively. L and M are the length of the substrate and mass of the device per unit area. The amplitude and angular frequency of the applied excitation is given by u_0 and Ω respectively. x and t are the spatial coordinates and time

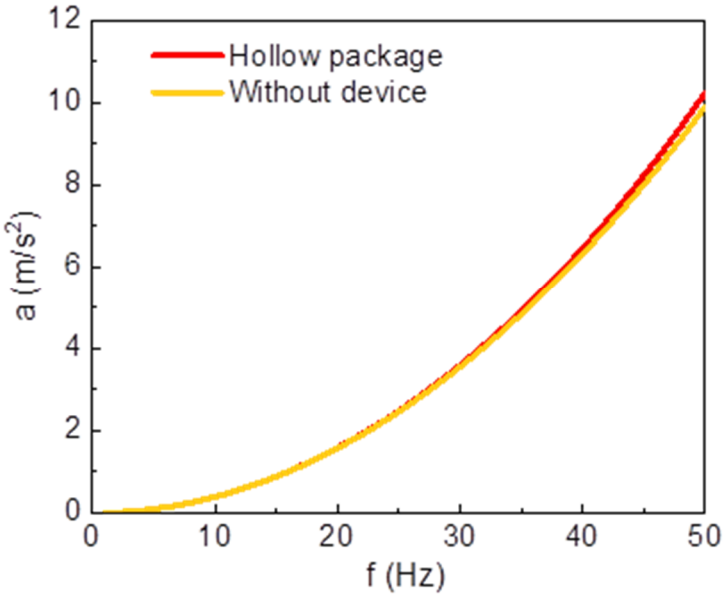

Fig. S8.The acceleration of the elastomer as a function of the applied frequency for the hollow package and without a device. The parameters used in the simulation are E = 60 kPa, ρ = 1070 kg/m^3, L = 2 mm, M_{hollow}=0.01 g/mm^2 which represents the weight of the device over the area of its bottom layer, u_0 = 0.1 mm, and the damping ratio (ξ= ηω) was 0.03.

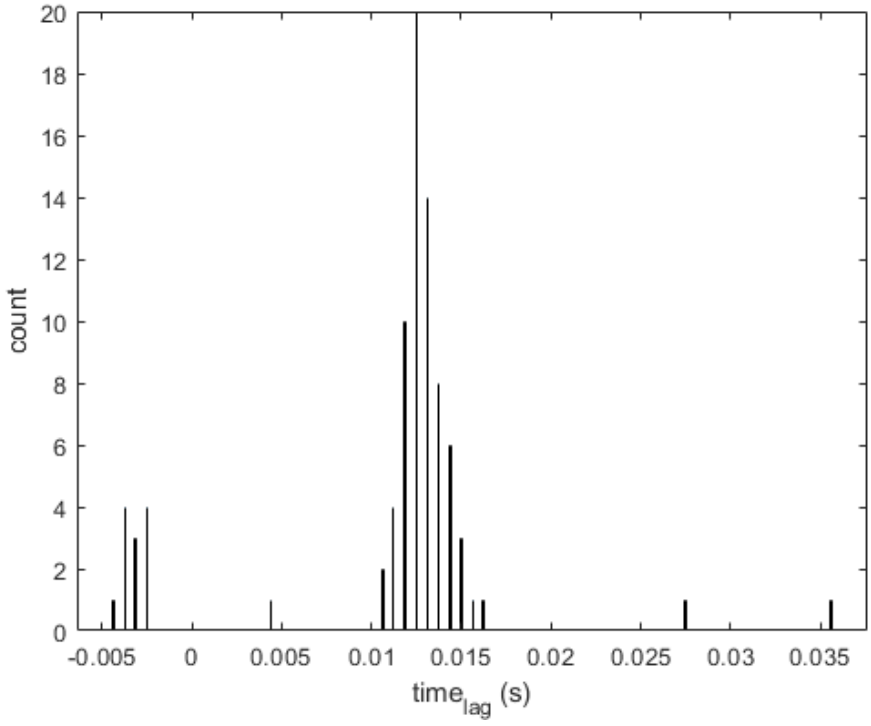

Fig. S9. Histogram of the time lag results from cross correlations between the pulses from the suprasternal notch (SN) and from the chest. The SN has the time lag of ~13 ms. This indicates that the vibratory signatures related to the pulsatile flow of blood are from the carotid artery as opposed to chest/body vibrations due directly to the heartbeat.

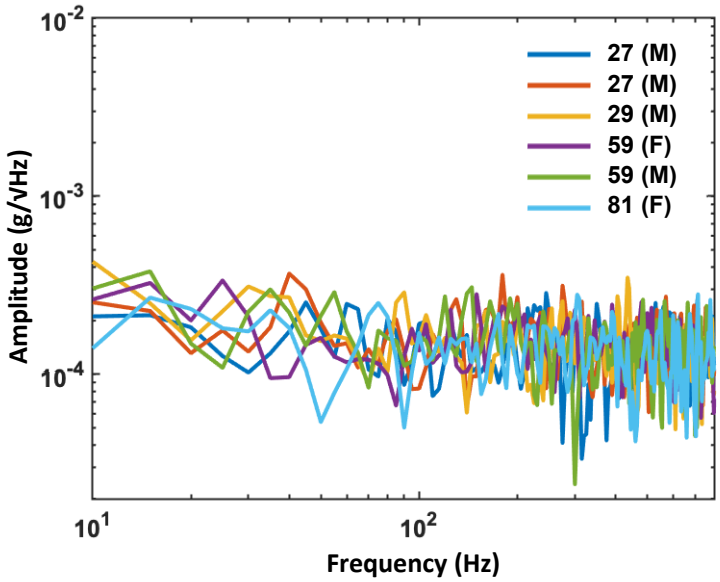

Fig. S10. Short-time windowed (0.2 s) spectrum of z-axis acceleration measured from the SN of five subjects across different ages and genders. Data from male (M) and female (F) subjects from 27 to 81 years old, each while sitting quietly in a resting state. The analysis windows are manually chosen from time periods where no bio-signals are clearly present. The spectrums indicate a noise behavior of the device close to that on the Ecoflex (Fig. 2a), which exhibit no clear difference between different age groups.

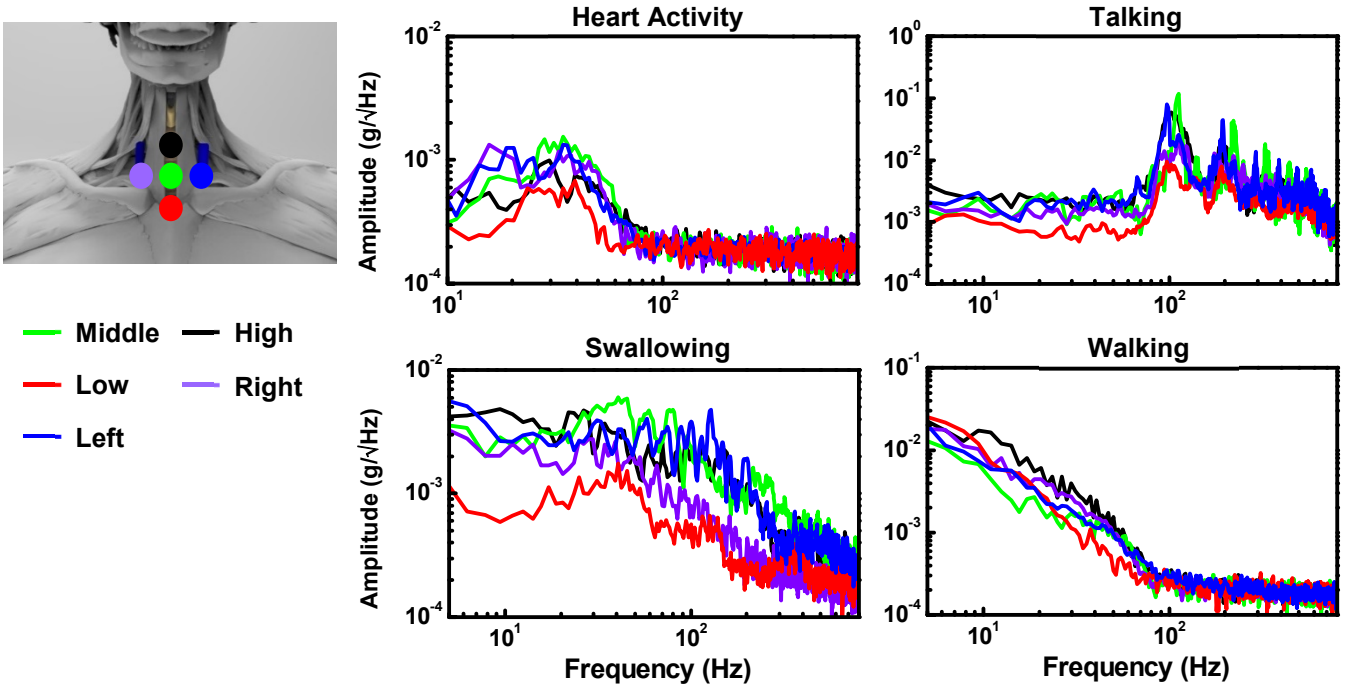

Fig. S11. Demonstration of the effect of mounting location. The measurements are from five different locations (+/- 1 cm vertical and horizontal displacements from the center of the SN) of a male subject with lower body mass. The results indicate that the device is not sensitive to the mounting locations, especially for the prominent frequency range for each distinctive event. There are slight differences in the magnitude of the signal relative to the position which agrees with the anatomical locations of the associated signal sources.

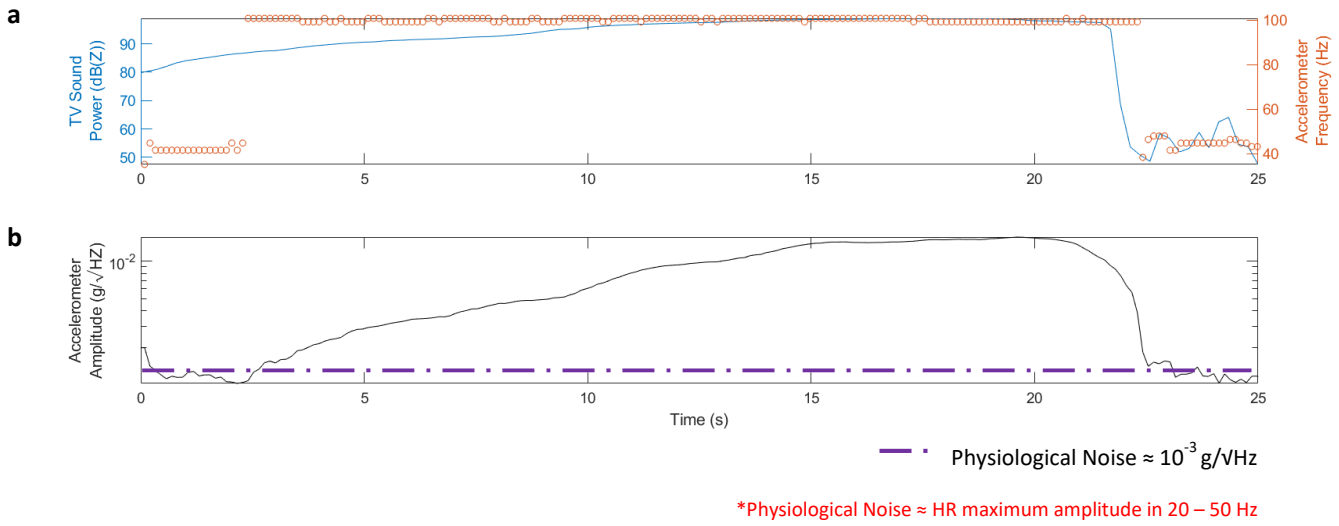

Fig. S12. Device sensitivity test to 100 Hz ambient TV sound. (a) The device is responsive to ambient sound that is louder than 87 dBZ, which was measured by the microphone. **(b)** Even though the device picks up the ambient sound starting at 87 dBZ, its effect in the accelerometer amplitude is not significant until it reaches 98 dBZ. Even when the ambient sound reaches the power of 98 dBZ, the accelerometer amplitude ($2x10^{-2}$ g/√Hz) is smaller than that of the general speech signal (10^{-1} g/√Hz).

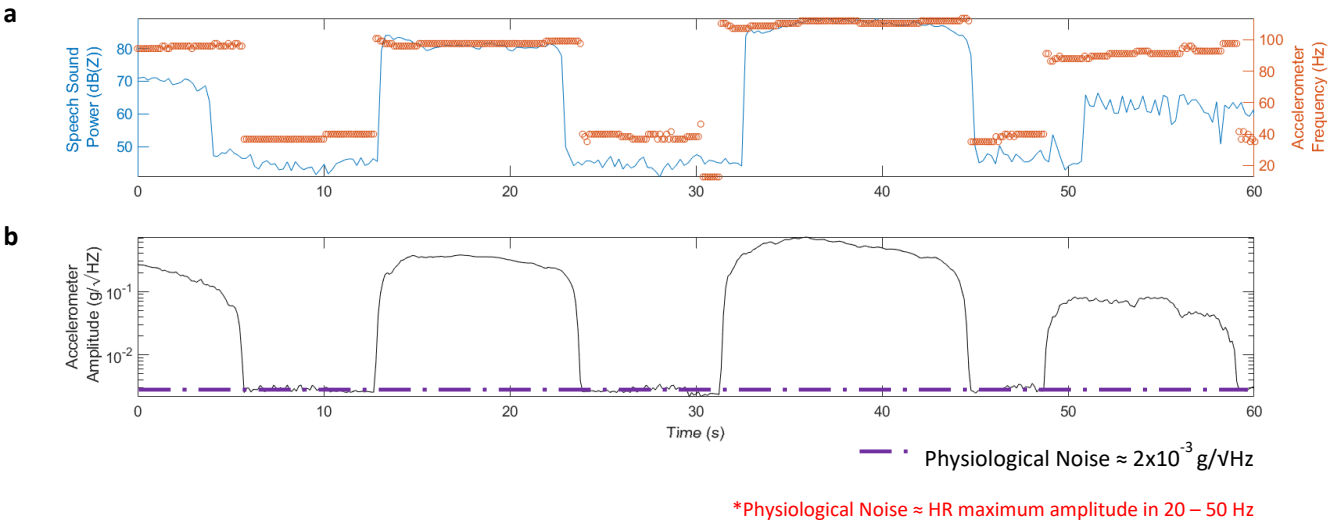

Fig. S13. Device sensitivity test to vocal sound. (a) The device is sensitive to vocal sound that is softer than 65 dBZ, which was measured by the microphone. **(b)** Even when the vocal sound is ~65 dBZ, the device picks up the vocal fold vibration with the adequate amplitude (10^{-1} g/√Hz) for the signal processing algorithm.

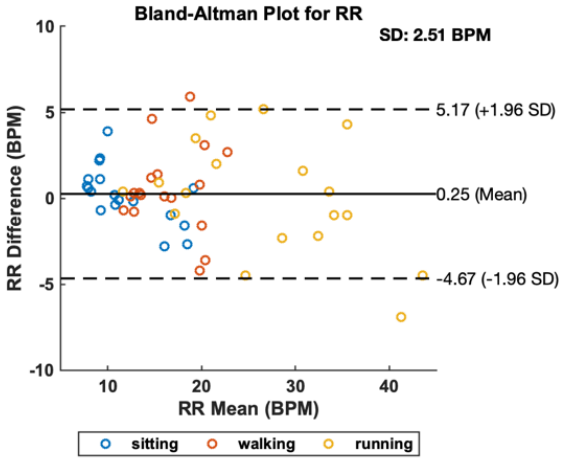

Fig. S14. Bland-Altman analysis for RR under different activities. For sitting, the mean difference between MA and reference measurements is 0.21 BPM and the standard deviation A_{RMS} = 1.63 BPM (N=18); for walking, the mean difference is 0.52 BPM, and A_{RMS} = 2.43 BPM (N=19); for running, the mean difference is 0.01 BPM and A_{RMS} = 3.34 BPM (N=19). N indicates the sample size for each scenario.

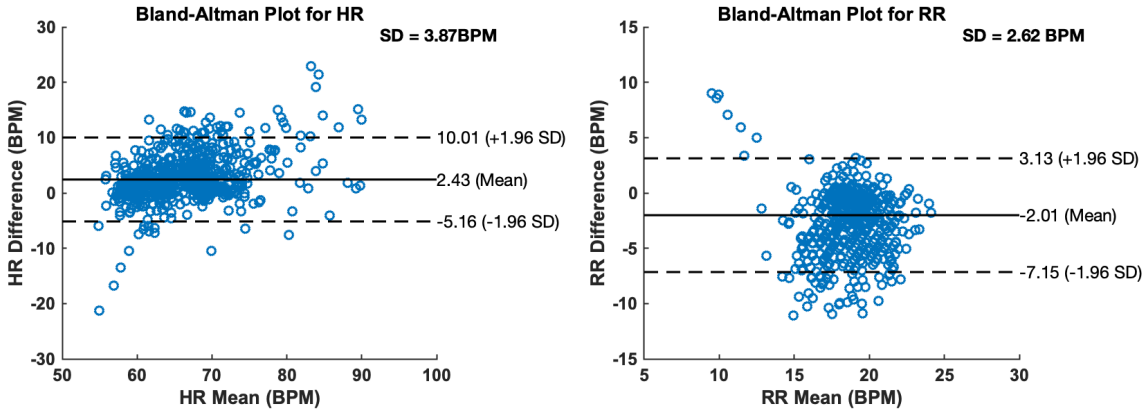

Fig. S15. Bland-Altman analysis for HR and RR during the 7 h sleep study. HR has a mean difference of 2.4 BPM and a standard deviation A_{RMS} of 3.9 BPM (N = 853). RR has a mean difference of -2.0 BPM and a standard deviation of 2.6 BPM (N = 853). N indicates the sample size for each scenario.

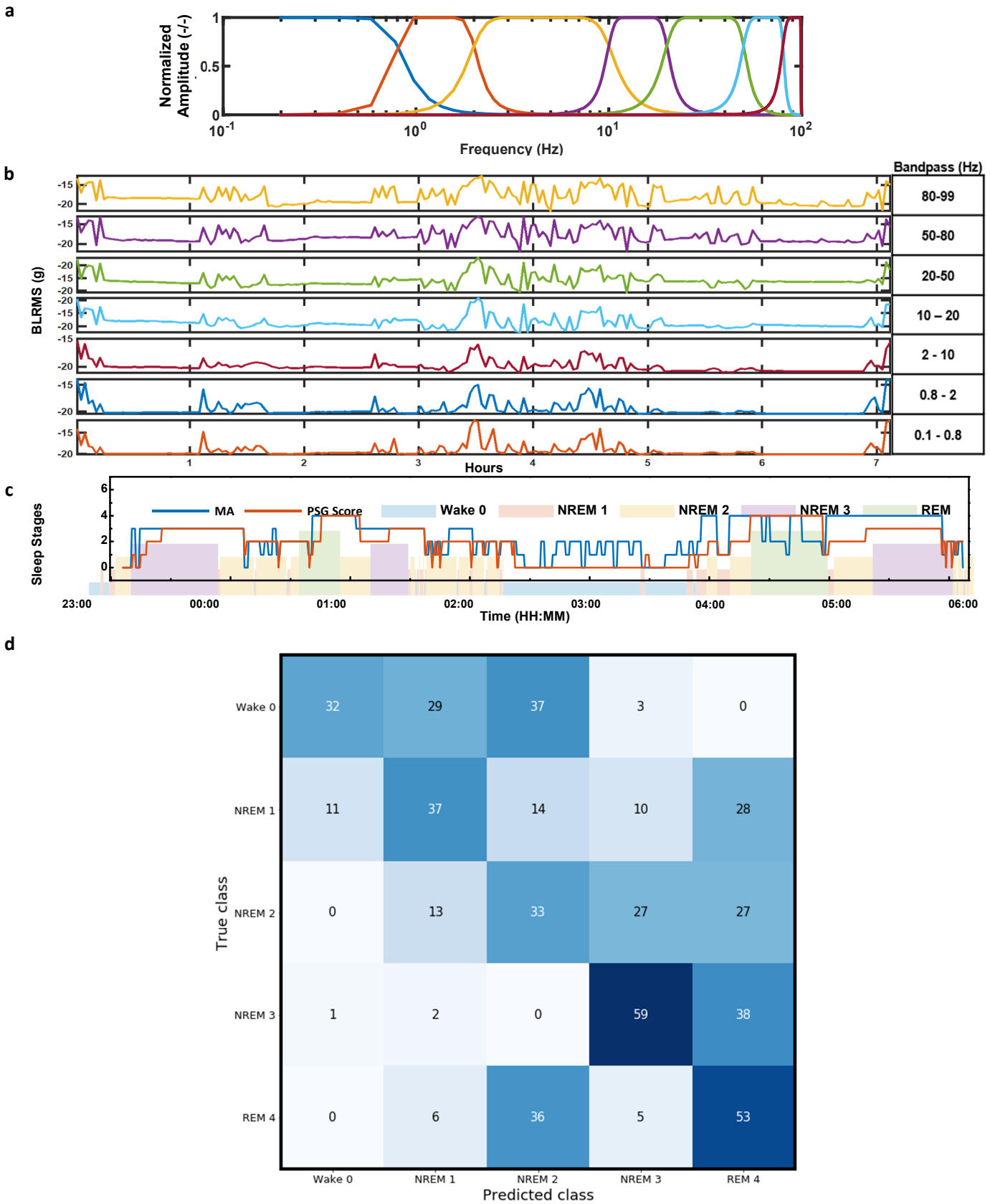

Fig. S16. Feature extraction and classification of sleep stages. (a) The filter-bank for energy feature generation **(b)** The time series of multi-band energy extracted from z-axis acceleration measurements. **(c)** The inference of sleep stages based on the multi-band signal power in comparison with clinically determined sleep stages. **(d)** The confusion matrix for the success rate of the classification.

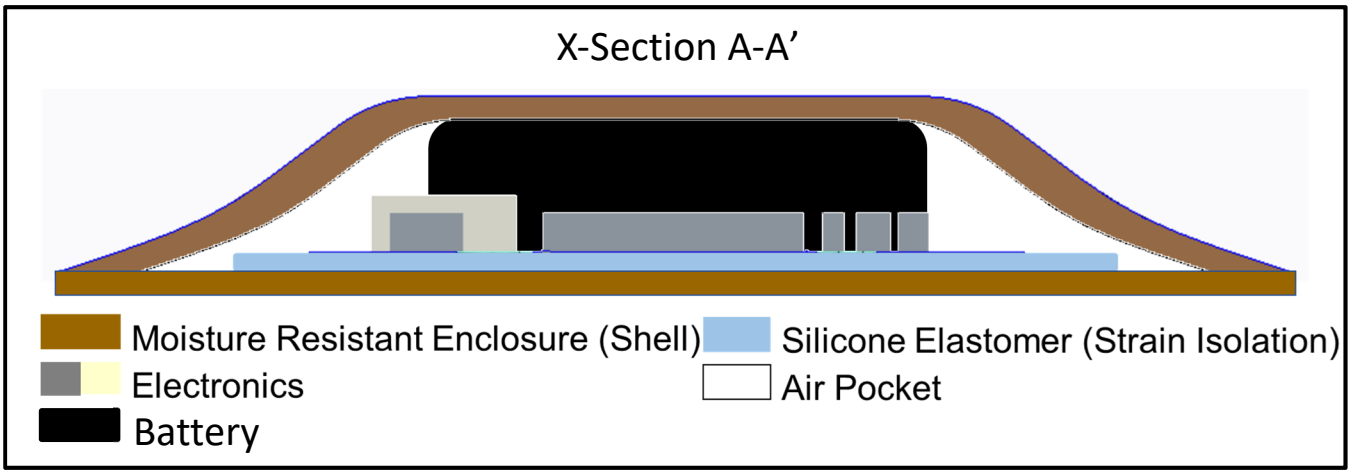

Fig. S17. Cross-sectional schematic illustration of the architecture of the system. A thin membrane (300 μm) of a low modulus formulation of silicone (Ecoflex) forms an air pocket, or hollow enclosure. The hollow enclosure construction minimizes mechanical constraints of the serpentine interconnects during the device deformations.

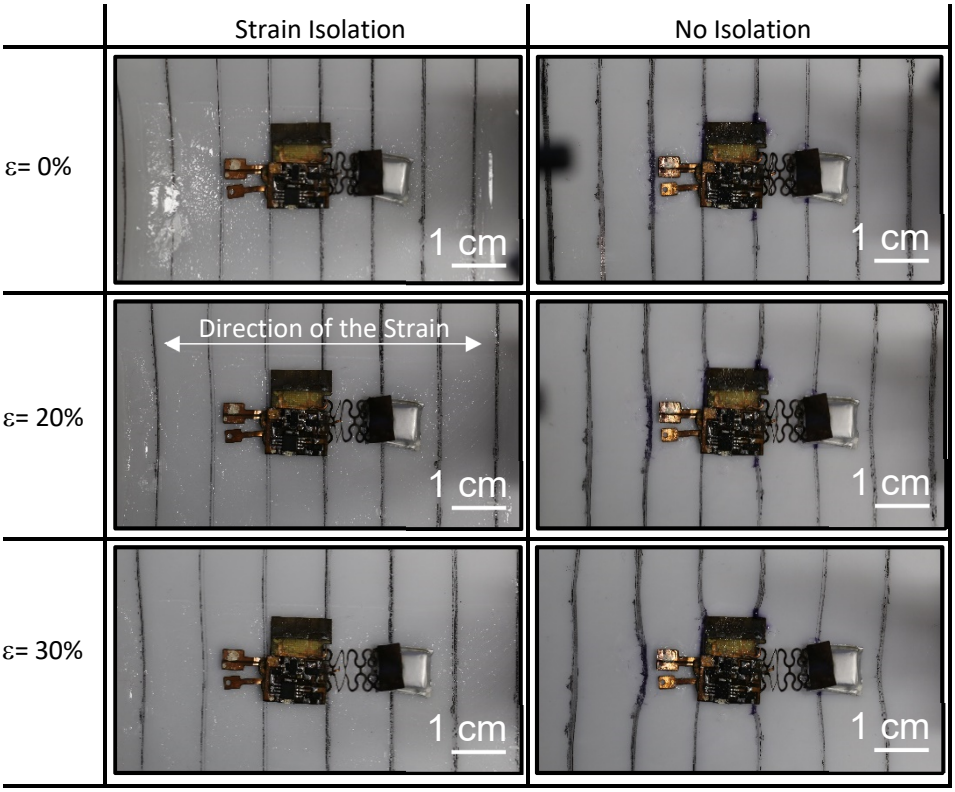

Fig. S18. Demonstration of the effect of strain isolation. Devices with and without strain isolation are mounted to an underlying silicone elastomer with vertical line markings to illustrate the effect of the strain isolation layer. Strain isolation minimizes deformations in the silicone elastomer that otherwise results from the rigid islands that support the electronic components.

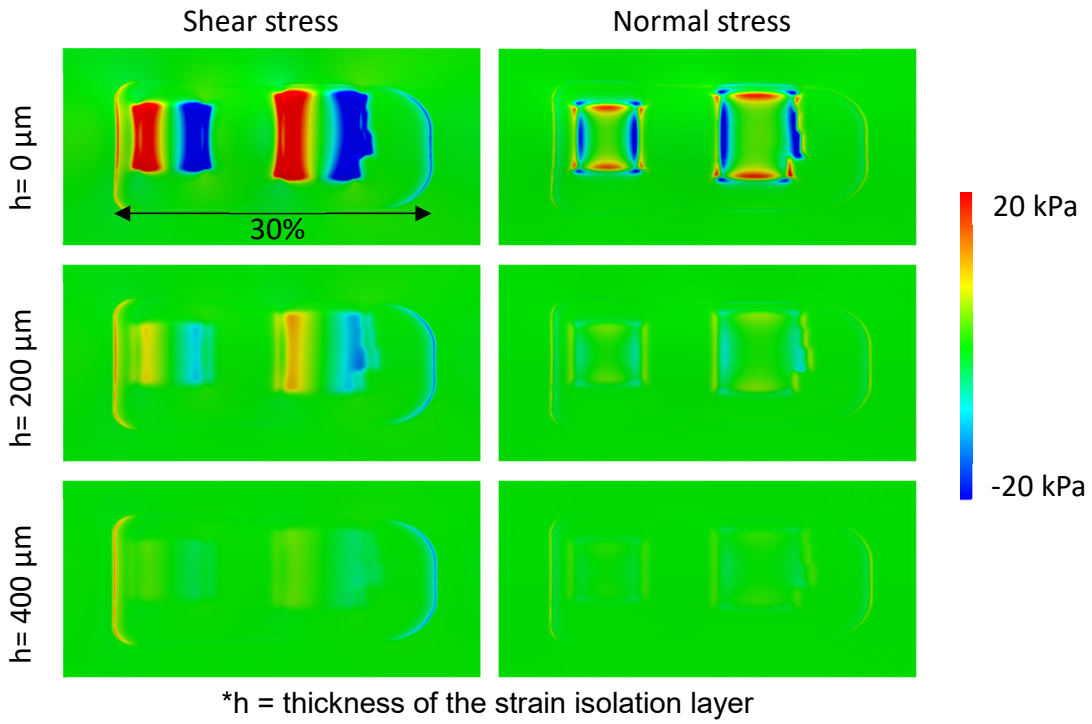

Fig. S19. The stress distributions on the skin with a strain isolation layer. The color indicates stress on the skin induced by stretching the device by 30% when different strain isolation layer thicknesses (h = 0, 200, and 400 µm) are used.

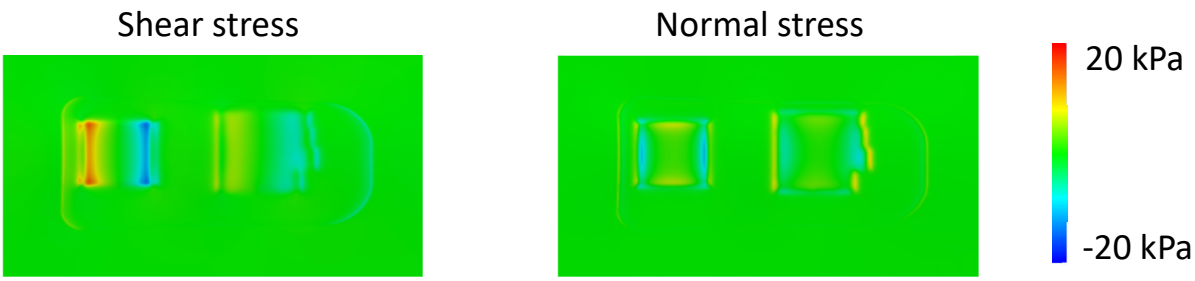

Fig. S20. The stresses on the skin from the 10% stretched device without a strain isolation layer. The device without the strain isolation layer induces stress on the skin even at low tensile strain.

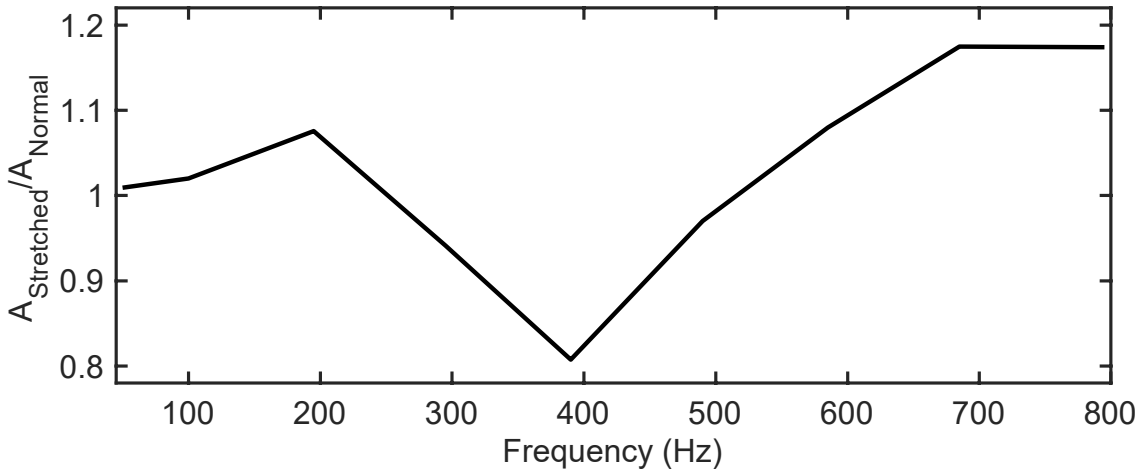

Fig. S21. Experimental comparison between the frequency responses of a normal device and a 12% stretched device. The ratio between the frequency response of a 12% stretched device $A_{Stretched}$ and that of a normal device A_{Normal} stays close to 1 across the frequency range (0-800 Hz) except for a maximum of ~20% drop around 400 Hz. The stretched device becomes more sensitive at high frequencies (>500 Hz). The stretched device also delaminates at a higher frequency (>295 Hz) and causes transient instability.

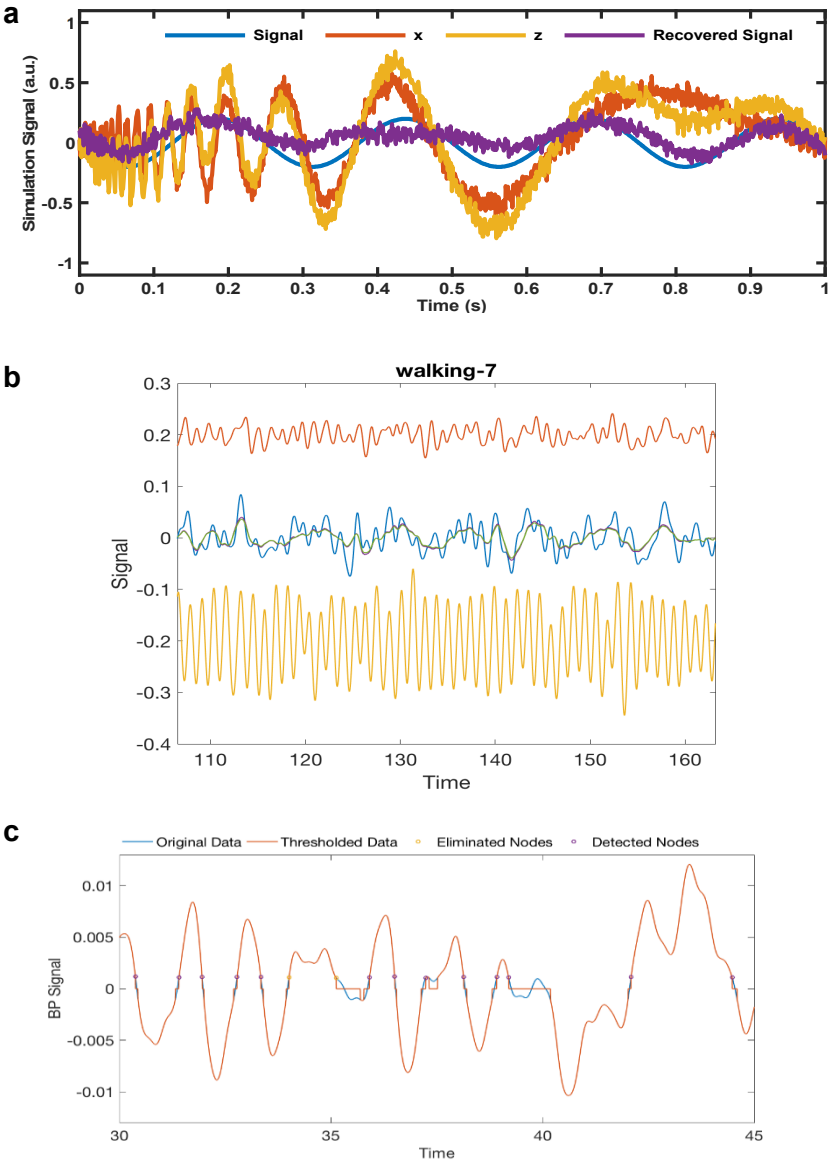

Fig. S22. Applying CWT subtraction methods to simulation and experimental signal. (a) A numerical simulation test for performance of wavelet cross spectrum analysis. The algorithm detects the common mode (a large amplitude chirp) between X and Z and recovers the differential sinusoidal signal embedded in Z. **(b)** A sample wavelet cross spectrum analysis for chest-wall motion decoupling using three-axis acceleration measurements. The 0.1-1 Hz band-passed x- and y-axis data is offset by 0.2 g for visualization purposes. **(c)** Zero-crossing nodes detected from the extracted signal. A dynamic threshold equal to a tenth of the standard deviation of 1 min data eliminates the effects of small-amplitude ripples that appear on top of the general respiration pattern.

Table S1. The demographic and sample size information of all participants.

Cycling	Respiration	Dining
Subject 1 (N=60)	Subject 1 (N=18)	Subject 1 (N=5)
Subject 2 (N=60)	Subject 2 (N=10)	Subject 2 (N=6)
Subject 3 (N=60)	Subject 3 (N=7)	Subject 3 (N=4)
Subject 4 (N=60)	Subject 6 (N=12)	Subject 4 (N=6)
Subject 5 (N=61)	Subject 7 (N=5)	Subject 8 (N=5)

Subject	Age	Gender	Race	Ethnicity
Subject 1 (David)	21	Male	Asian	Filipino-Chinese
Subject 2 (Xiaoyue)	28	Female	Asian	Chinese
Subject 3 (Mohan)	26	Female	Asian	Chinese
Subject 4 (Peter)	26	Male	Asian	Korean
Subject 5 (Jiahong)	22	Male	Asian	Chinese
Subject 6 (Marc)	21	Male	Black	Afro-Puerto Rican
Subject 7 (Esther)	21	Female	Asian	Korean
Subject 8 (Jeremy)	20	Male	White	Argentine American